

Electronic Supplementary Information

A General Approach for Nanoparticle Composite Transport

Materials toward Efficient Perovskite Solar Cells

*Yihua Chen^a, Jianjun Gu^a, Rundong Fan^a, Ziliang Li^a, Liang Li^a, Ligang Wang^a,
Guanhaojie Zheng^a, Honggang Nie^c, Qi Chen^b and Huanping Zhou^{a,b,*}*

a Department of Materials Science and Engineering, Department of Energy and Resources Engineering, College of Engineering, Peking University, Beijing 100871, P.R.China.

b School of Materials Science and Engineering, Beijing Institute of Technology, Beijing 100081, P. R. China.

c Beijing National Laboratory for Molecular Sciences, Key Laboratory of Bioorganic Chemistry and Molecular Engineering of Ministry of Education, College of Chemistry, Peking University, Beijing 100871, P.R.China.

* Corresponding Author: happy_zhou@pku.edu.cn

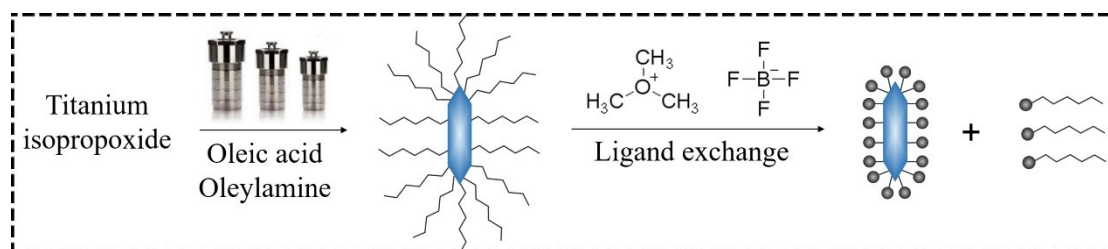


Fig. S1 The schematic illustration of the synthetic process and modification mechanism of the TiO₂ nanocrystals obtained from hydrothermal approach.

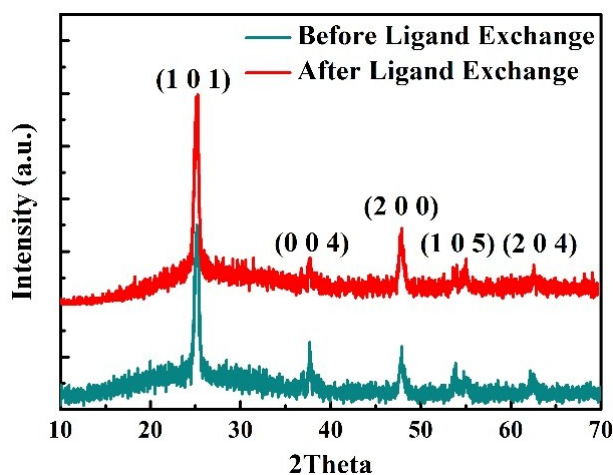


Fig. S2 X-ray diffraction patterns of the hydrothermally synthesized TiO₂. A set of strong peaks located at 25.3°, 37.8°, 48.0°, 53.9°, 62.7° were assigned to be (101), (004), (200), (105), and (204) of anatase TiO₂, respectively.

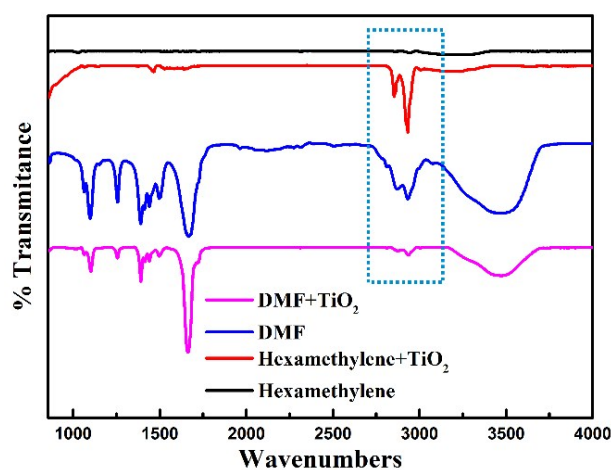


Fig. S3 Fourier transform infrared spectra of TiO₂ solutions before and after ligand exchange.

The long chain aliphatic hydrocarbon (most likely the oleate)-passivated TiO₂ nanocrystals synthesized in a solvent system of oleic acid and oleylamine, are highly insulating and constituting a significant barrier for charge transport in devices.

BF_4^- ligand can remove and exchange the native ligands from TiO_2 nanocrystals surface effectively, which have been discussed in the previous literature.¹ Furthermore, we have identified the ligand removed from the TiO_2 surface based on FTIR spectroscopy measurement, which is shown in **Fig S3**. As expected, oleate-passivated TiO_2 exhibited strong signals around 2900 cm^{-1} before ligand exchange, which is assigned to the symmetric and antisymmetric CH stretches from oleate ligands. After treatment with BF_4^- ligand, the signal around 2900 cm^{-1} was significantly decreased, indicating the removal of oleate ligand. The existence of the tiny peak around 2900 cm^{-1} may originate from the oleate ligand or DMF solvent residue. And the stretching band attributable to BF_4^- around 1080 cm^{-1} have not been observed, which is consistent with the previous literature.¹

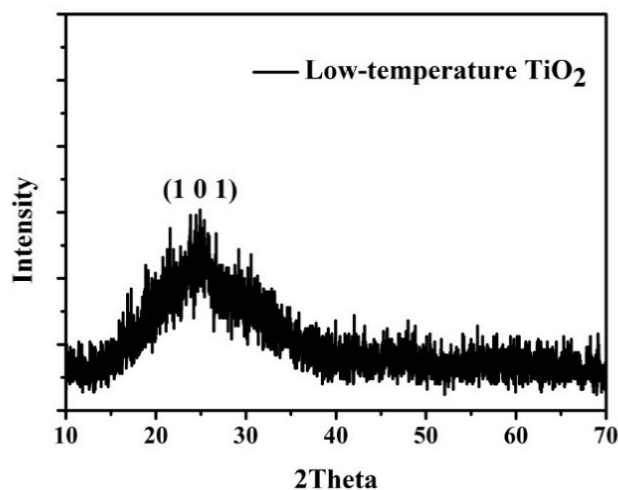


Fig. S4 The X-ray diffraction pattern of the low-temperature sol-gel synthesized TiO_2 .

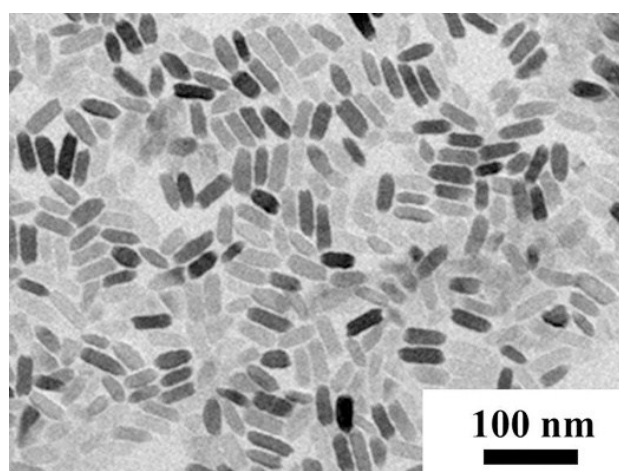


Fig. S5 The TEM image of the TiO_2 nanoparticles obtained from hydrothermal approach before ligand exchange.

Table S1 Performance of planar perovskite solar cells based on TiO₂ nanoparticles obtained from sol-gel or hydrothermal methods.

Device	V _{oc} (V)	J _{sc} (mA/cm ²)	FF	PCE (%)
Standard TiO ₂	1.08	19.90	0.69	14.77
Hydrothermal TiO ₂	1.04	18.42	0.64	12.28

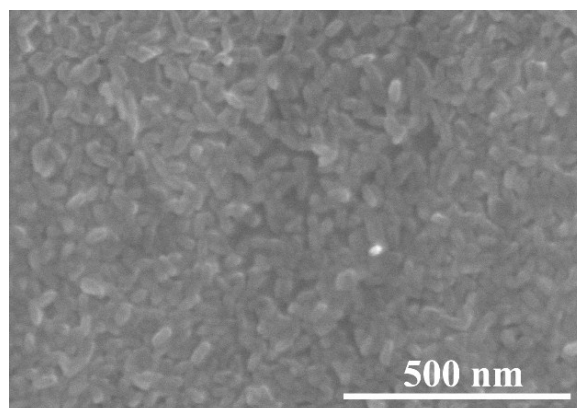


Fig. S6 The top view SEM image of the hydrothermal processed TiO₂ nanocrystals ETL on the ITO substrate.

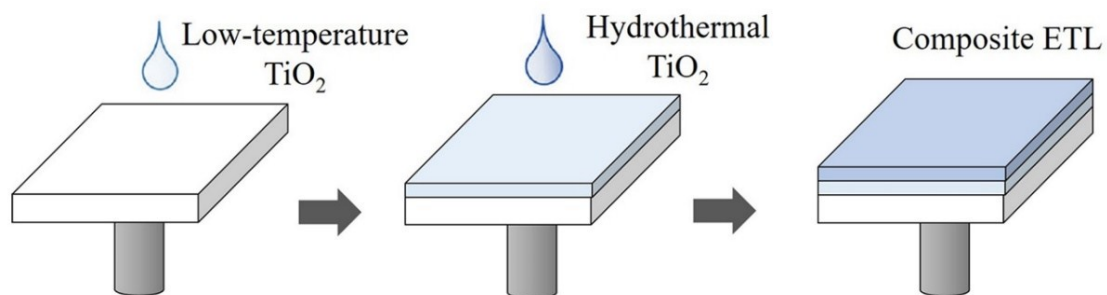


Fig. S7 The Schematic image of the procedure for preparing the composite TiO₂ electron transport layer.

Table S2 Performance characteristics of planar perovskite solar cells based on standard and composite TiO₂ ETLs.

ETL	Sweep direction	V _{oc} (V)	J _{sc} (mA/cm ²)	FF	PCE (%)	Hysteresis index
Standard TiO ₂	Reverse	1.10	20.88	0.74	17.04	0.316
	Forward	1.06	19.53	0.55	11.30	
Composite TiO ₂	Reverse	1.11	21.98	0.78	19.14	0.278
	Forward	1.08	19.54	0.63	13.23	

The hysteresis index was defined as:

$$\text{Hysteresis Index} = \frac{J_{RS}(0.8V_{oc}) - J_{FS}(0.8V_{oc})}{J_{RS}(0.8V_{oc})}$$

where the $J_{RS}(0.8V_{oc})$ and $J_{FS}(0.8V_{oc})$ represented the current density at 80% of the open voltage for the reserve scan (RS) and forward scan (FS) respectively.

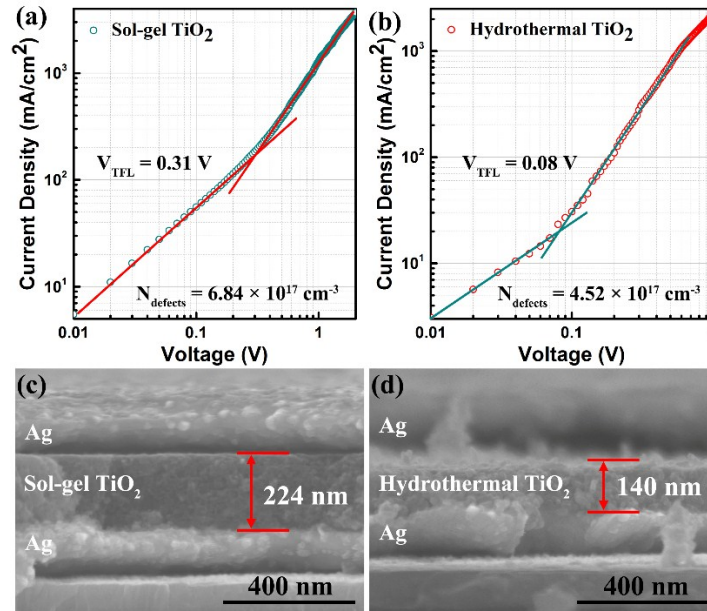


Fig. S8 (a) and (b) Space charge limited current test for Ag/TiO₂/Ag devices to estimate the defect density of TiO₂. (c) and (d) The SEM images for the cross section of Ag/TiO₂/Ag devices used in the space charge limited current test.

To quantify the defects density of standard TiO₂ and composite TiO₂ films, we fabricated specific device by sandwiching hydrothermal or sol-gel TiO₂ between silver and silver electrode, and recorded using the space charge limited current (SCLC) method, which is shown in **Fig. S8**. The transition points correlates to a trap-filled limit, which was determined by the trap-state density.

$$N_{defects} = 2\epsilon\epsilon_0V_{TFL}/eL^2$$

where e is the elementary charge, L is the thickness, ϵ is the dielectric constants and ϵ_0 is the vacuum permittivity of the TiO₂ film. The thickness was confirmed to be 224 nm

and 140 nm for sol-gel and hydrothermal TiO₂, respectively, by the cross sectional SEM images for the Ag/TiO₂/Ag devices. To be noted, the TiO₂ films fabricated in the SCLC test were thick enough to ensure the accuracy of the SCLC and SEM measurements. According to previous literature,² we assumed a dielectric of 100 for the TiO₂. The values of $N_{defects}$ were estimated to be $6.84 \times 10^{17} \text{ cm}^{-3}$ and $4.52 \times 10^{17} \text{ cm}^{-3}$ for sol-gel TiO₂ film and hydrothermal TiO₂ film respectively, which reasonably demonstrated that composite TiO₂ film exhibited fewer trap density than standard TiO₂ film.

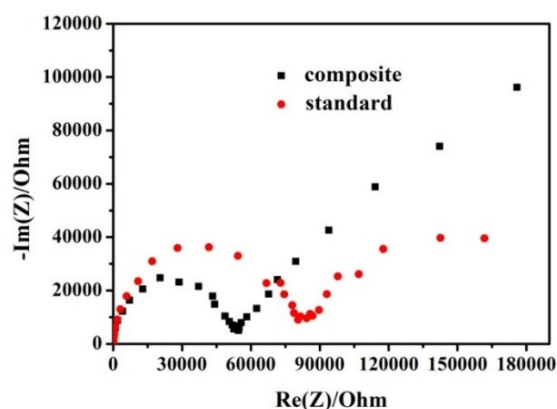


Fig. S9 Electrochemical impedance spectroscopies (EIS) of devices based on standard and composite TiO₂ ETLs.

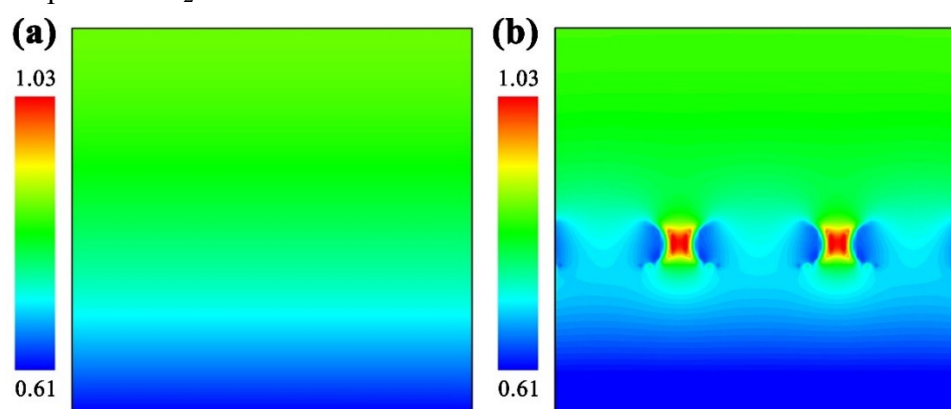


Fig. S10 The simulation profiles of (a) the standard TiO₂/perovskite and (b) composite TiO₂/perovskite.

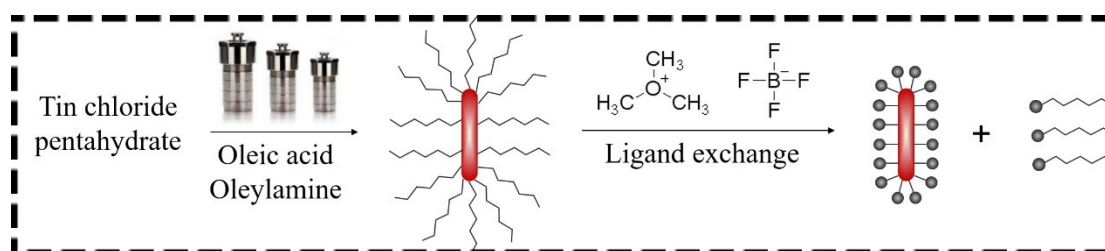


Fig. S11 Schematic illustration of the synthetic process and modification mechanism of the SnO₂ nanocrystals obtained from hydrothermal approach.

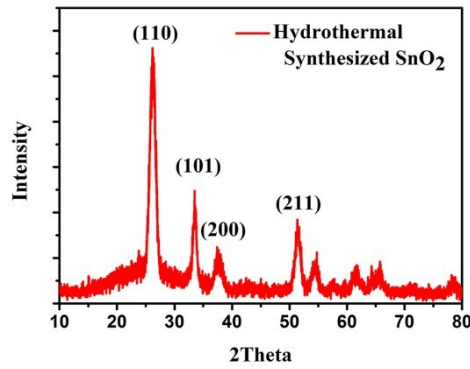


Fig. S12 X-ray diffraction patterns of the SnO₂ nanoparticles obtained from the hydrothermal approach. The XRD pattern indicated that the SnO₂ nanorods were tetragonal phase with high crystallinity.

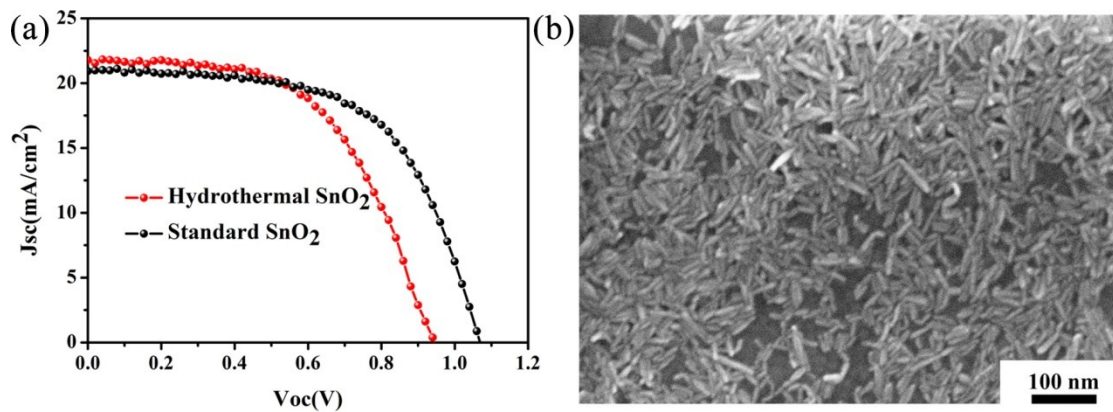


Fig. S13 (a) J - V curves of devices based on standard SnO₂ and hydrothermal SnO₂ nanorods. (b) The top view SEM image of the hydrothermal processed SnO₂ nanocrystals ETL.

Devices only employing the hydrothermal SnO₂ nanorods as ETL showed an obviously decreased V_{OC} and fill factor, when compared to the standard sample based on the sol-gel processed SnO₂ film prepared from SnCl₂·2H₂O ethanol solution as shown in **Figure S13a** and **Table S3**. This could also be resulted from the poor film coverage of the hydrothermal SnO₂ nanorods, leading to the direct contact for the ITO substrate with perovskite. The corresponding SEM image was shown in **Figure S13b**.

Table S3. Performances of perovskite solar cells based on standard SnO₂ and hydrothermal SnO₂ nanorods.

Device	V_{OC} (V)	J_{SC} (mA/cm ²)	FF	PCE (%)
Standard SnO ₂	1.07	21.25	0.60	13.61
Hydrothermal SnO ₂	0.94	21.21	0.57	11.45

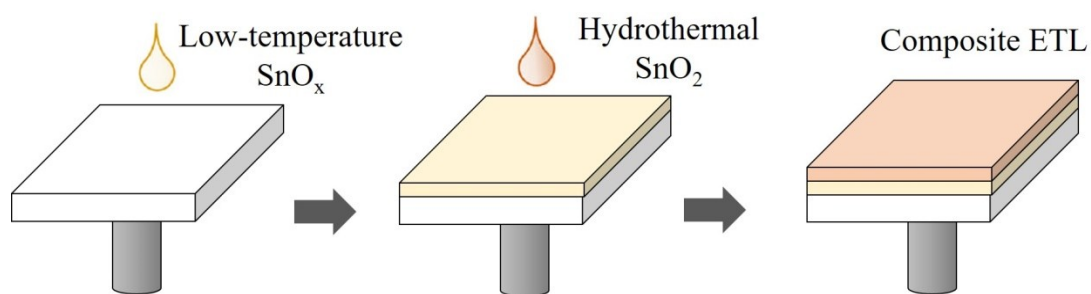


Fig. S14 Schematic image of the procedure for preparing the composite SnO₂ electron transport layer.

Table S4. Performance characteristics of planar perovskite solar cells based on standard and composite SnO₂ ETLs.

ETL	Sweep direction	V _{oc} (V)	J _{sc} (mA/cm ²)	FF	PCE (%)	Hysteresis index
Standard SnO₂	Reverse	1.08	21.51	0.73	17.01	0.407
	Forward	1.06	21.35	0.56	12.68	
Composite SnO₂	Reverse	1.06	22.32	0.77	18.10	0.055
	Forward	1.03	22.06	0.73	16.59	

The hysteresis index was defined as:

$$\text{Hysteresis Index} = \frac{J_{RS}(0.8V_{oc}) - J_{FS}(0.8V_{oc})}{J_{RS}(0.8V_{oc})}$$

where the $J_{RS}(0.8V_{oc})$ and $J_{FS}(0.8V_{oc})$ represented the current density at 80% of the open voltage for the reserve scan (RS) and forward scan (FS) respectively.

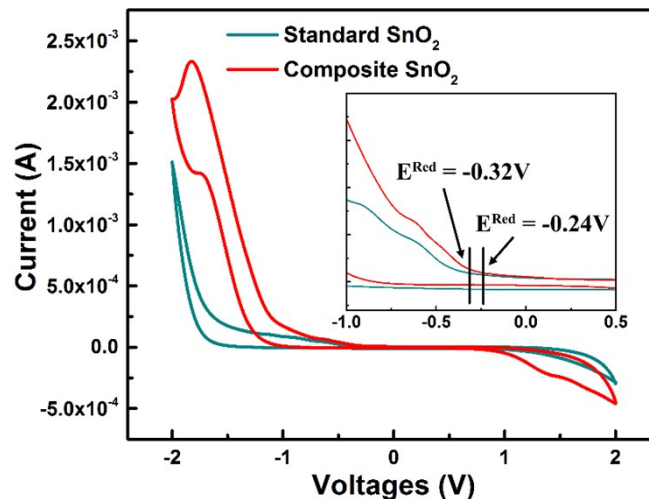


Fig. S15 Cyclic voltammetry (CV) curves of the standard SnO₂ and composite SnO₂ films, the reference electrode is saturated calomel electrode.

The V_{OC} of SnO₂ based device has a slight drop indeed when compared to the standard device. To address this issue, we further conducted cyclic voltammetry (CV) test for standard and composite SnO₂ films, which is shown in **Fig. S15**. The conduction-band minimum (CBM) of as-prepared standard and composite SnO₂ ETL were 4.42 and 4.50 eV respectively, ($E_{CBM} = eE^{Red} + 4.5 + 0.24$ eV, the reference electrode is saturated calomel electrode). The relatively lower CBM of the composite SnO₂ ETL, probably lead to a decreased quasi-Fermi level splitting that associated to the slight drop of V_{OC} .

Experimental Section

Synthesis of TiO₂ nanocrystals: The traditional low-temperature processed TiO₂ nanocrystals were obtained from a non-hydrolytic sol-gel approach in the ambient air and stabilized with Tiacac (Aldrich) which was widely used in literatures.³ In the typical synthesis of hydrothermal TiO₂ nanocrystals, 1.71 mL tetrabutyl titanate (Chengdu Xiya Chemical Co. Ltd.) and 1.48 mL titanium isopropoxide (Aladdin) were added into a mixed solution of 6.34 mL oleic acid (Aldrich), 9.70 mL oleylamine (Aldrich), and 2.915 mL absolute ethanol with stirring. Then the mixed solution was added 9.5 mL ethanol and 0.5 mL DI water and transferred into a Teflon reactor. Then the reactor was kept at 180 °C for 18 h and naturally cooled down to room temperature. The as-obtained precipitates were re-dissolved in 20 mL hexamethylene and centrifuged with the addition of 20 mL ethanol. This procedure was repeated for two times and the final TiO₂ nanocrystals were collected and dispersed in 20 mL hexamethylene.

Synthesis of SnO₂ nanocrystals: In the typical synthesis of hydrothermal SnO₂ nanocrystals, 175.3 mg tin(IV) chloride pentahydrate (Kermel Chemical Co. Ltd.) were added into a mixed solution of 4.76 mL oleic acid (Aldrich) and 1.61 mL oleylamine

(Aldrich). Then the mixture was kept at 100 °C for 30 min with stirring in vacuum until the mixture became clear and transparent. 68.1 mg sodium dodecyl sulfonate (SDS) (Xilong Chemical Co. Ltd.) and 25 mL DI water were added when the solution was transferred into a Teflon reactor. Then the reactor was kept at 220 °C for 24 h and naturally cooled down to room temperature. The as-obtained precipitates were re-dissolved in 5 mL hexamethylene and centrifuged with the addition of 20 mL ethanol. The final SnO₂ nanocrystals were collected and dispersed in 5 mL hexamethylene.

Method of ligand exchange: 100 mg TiO₂ or SnO₂ nanoparticles (centrifuged and dried from the above TiO₂/hexamethylene or SnO₂/hexamethylene solution) was dissolved in 4 mL n-hexane with stirring for 10 min. Then 6 mL Trimethyloxonium tetrafluoroborate (TEOTB) (Aldrich) in DMF with a concentration of 20 mg/mL was added into the solution and stirred for about 1 h. After that, the as-obtained product was centrifuged with addition of 10 mL dichloromethane and dispersed in 4 mL DMF with a concentration of 25 mg/mL.

Device fabrication: The planar perovskite solar cells were fabricated on ITO glass which was sequentially washed with distilled water, ethanol, acetone and isopropanol. The TiO₂ compact layer was prepared by spin coating the sol-gel or hydrothermally synthesized TiO₂ nanocrystal solution, and annealed at 150 °C for 30 min in air. The SnO₂ compact layer was prepared by spin-coating the SnCl₂ ethanol solution or hydrothermally synthesized SnO₂ nanocrystal solution, and annealed at 180 °C for 1 h in air. The standard ETL was based on double TiO₂ or SnO₂ compact layers (spin-coated 3000 rpm 30 s), whereas the composite ETL was based on one layer of sol-gel synthesized TiO₂ or SnO₂ (spin-coated 5000 rpm 30 s) and one layer of hydrothermally synthesized TiO₂ or SnO₂ layer (spin-coated 3000 rpm 30 s). To fabricate the perovskite layer, the two step inter-diffusion method was used. A solution of PbI₂ (Alfa Aesar) in DMF with concentration of 450 mg/mL and CH₃NH₃I in isopropanol with concentration of 50 mg/mL was sequentially spin coated on the substrate at 3000 rpm. The PbI₂ layer was annealed at 90 °C for 10 min in the glovebox while the perovskite layer was annealed at 150 °C for 15 min in the air. The Spiro-MeOTAD (Luminescence Tech.) in chlorobenzene (80 mg/mL) solution with 17.5 μL Li-bis(trifluoromethanesulfonyl)imide (Li-TFSI) /acetonitrile (520 mg/mL) and 30 μL tert-butylpyridine (tBP) was spin-coated on top of the perovskite layer at 3000 rpm to form the HTM layer. Finally, a 100 nm gold electrode was vacuum-deposited under a pressure of 1.5×10^{-4} Pa.

Characterization: The X-ray diffraction (XRD) data were obtained from a Bruker D8 Advance X-ray diffractometer using filtered Cu K α ($\lambda = 1.5405 \text{ \AA}$) radiation. The TEM images were taken on a Tecnai G2 F20 with an accelerating voltage of 200 kV. The SEM images were obtained from a S4800 scanning electron microscope. PL and TRPL testing were based on the FLS980 (Edinburgh Instruments Ltd) with an excitation at

470 nm. The UV–vis absorption spectra of the samples was obtained by an UV–visible diffuse reflectance spectrophotometer (UV–vis DRS, Japan Hitachi UH4150). The J-V curves were measured using a Keithley 2400 source-measure unit under AM 1.5G illumination at 100 mW/cm² provided by a Oriel Sol2A solar simulator in ambient air. Light intensity was calibrated with a KG 5 filtered Si reference cell which was calibrated by the National Institute of Metrology in China. A mask was used to define the device illumination area, which were fixed at 0.102 cm².

Notes and references

- 1 E. L. Rosen, R. Buonsanti, A. Llodes, A. M. Sawvel, D. J. Milliron and B. A. Helms, *Angew. Chem. Int. Ed. Engl.* 2012, **51**, 684.
- 2 K. Wojciechowski, M. Saliba, T. Leijtens, A. Abate and H. J. Snaith, *Energy Environ. Sci.* 2014, **7**, 1142.
- 3 H. P. Zhou, Q. Chen, G. Li, S. Luo, T.-B. Song, H.-S. Duan, Z. Hong, J. B. You, Y. Liu, Y. Yang, *Science* 2014, **345**, 542.